PHYSICAL REVIEW D **78,** 043506 (2008)

Antideuteron fluxes from dark matter annihilation in diffusion models

F. Donato[*]
Dipartimento di Fisica Teorica, Università di Torino, Istituto Nazionale di Fisica Nucleare, via P. Giuria 1, I-10125 Torino, Italy

N. Fornengo[+]
Dipartimento di Fisica Teorica, Università di Torino, Istituto Nazionale di Fisica Nucleare, via P. Giuria 1, I-10125 Torino, Italy

D. Maurin[‡]
Laboratoire de Physique Nucléaire et Hautes Energies,
CNRS-IN2P3/Université Paris VI et VII, 4 Place Jussieu, Tour 33, 75252 Paris Cedex 05, France
(Received 27 March 2008; published 4 August 2008)

Antideuterons are among the most promising galactic cosmic-ray-related targets for dark matter indirect detection. Currently only upper limits exist on the flux, but the development of new experiments, such as GAPS and AMS-02, provides exciting perspectives for a positive measurement in the near future. In this paper, we present a novel and updated calculation of both the secondary and primary $\bar{d}$ fluxes. We employ a two-zone diffusion model which successfully reproduces cosmic-ray nuclear data and the observed antiproton flux. We review the nuclear and astrophysical uncertainties and provide an up to date secondary (*i.e.* background) antideuteron flux. The primary (*i.e.* signal) contribution is calculated for generic weakly interactive massive particles (WIMPs) annihilating in the galactic halo: we explicitly consider and quantify the various sources of uncertainty in the theoretical evaluations. Propagation uncertainties, as is the case of antiprotons, are sizeable. Nevertheless, antideuterons offer an exciting target for indirect dark matter detection for low and intermediate mass WIMP dark matter. We then show the reaching capabilities of the future experiments for neutralino dark matter in a variety of supersymmetric models.

DOI: 10.1103/PhysRevD.78.043506 PACS numbers: 95.35.+d, 11.30.Pb, 12.60.Jv, 98.35.Gi

I. INTRODUCTION

The identification and the understanding of the nature of dark matter (DM) is one of the deepest open problems, together with the solution to the dark energy mystery, in the fundamental physics research. Many experimental efforts devoted to the detection of the astronomical dark matter in the halo of our and nearby galaxies have been carried out in underground laboratories, in large-area surface telescopes as well as in space. In the near future, the LHC will provide us with invaluable information on particle physics extending beyond the standard model, thus probing a wide class of theoretical models hosting the most viable DM candidates.

The indirect dark matter detection is based on the search for anomalous components due to the annihilation of DM pairs in the galactic halo, in addition to the standard astrophysical production of neutrinos, gamma rays and light antimatter in cosmic rays. Data on neutrinos, gamma rays, positrons and antiprotons are already available at a sensitivity level allowing some inspection on possible exotic contributions. In the seminal paper [1], it was proposed to look for cosmic antideuterons ($\bar{d}$) as a possible indirect signature for galactic dark matter. It was shown that the antideuteron spectra deriving from DM annihilation is expected to be much flatter than the standard astrophysical component at low kinetic energies, $T_{\bar{d}} \lesssim 2$–$3\ \mathrm{GeV/n}$. This argument motivated the proposal of a new space-borne experiment [2–4] looking for cosmic antimatter (antiproton and antideuteron) and having the potential to discriminate between standard and exotic components for a wide range of DM models. AMS-02 also has interesting capabilities of looking for cosmic antideuterons [5]. Antideuterons have not been measured so far, and the present experimental upper limit [6] is still far from the expectations on the secondary antideuteron flux which are produced by spallation of cosmic rays on the interstellar medium [7,8], but in fact perspectives for the near future are very encouraging.

In the present paper, we update and improve our calculation of the antideuteron primary flux in a full two-zone diffusion model, consistent with a number of independent cosmic-ray (CR) measurements, and explicitly estimate the uncertainties which affect the signal determination. In addition, we also provide a new determination of the secondary component. In Sec. II, the framework and ingredients for the solution of the two-zone transport equation are recalled. In Sec. III, the coalescence model for the nuclear fusion process is discussed both for secondary and primary $\bar{d}$ production. Section IV is dedicated to the sec-

---

[*] donato@to.infn.it
[+] fornengo@to.infn.it
[‡] dmaurin@lpnhe.in2p3.fr

ondary $\bar{d}$ flux and to the possible uncertainties affecting its evaluation. In Sec. V the production of antideuterons from DM particles is detailed and results on the propagated fluxes are presented, together with the estimation of the uncertainties due to propagation, to the dark matter halo profile and to the DM annihilation final states. Section VI demonstrates that antideuterons are probably one of the most powerful dark matter indirect detection channels, and shows the optimistic potentials of next-to-come balloon and space based missions. We finally draw our conclusions in Sec. VII.

II. THE PROPAGATION MODEL

Cosmic-ray fluxes are determined by the transport equation as given, e.g., in Berezinskii *et al.* [9]. If steady state is assumed, the transport equation for any nuclear species can be rewritten in terms of the cosmic-ray differential density $dn(\vec{r})/dE \equiv N(\vec{r})$ as

$$-\vec{\nabla}[K\vec{\nabla}N(\vec{r}) - \vec{V}_c N(\vec{r})] - \frac{\partial}{\partial E}\left[-f_{\rm o}N(\vec{r}) + s_{\rm o}\frac{\partial N(\vec{r})}{\partial E}\right] = Q_{\rm source}(\vec{r}) - n(\vec{r})v\sigma_{\rm ine}N(\vec{r}). \qquad (1)$$

The left-hand side (l.h.s.) describes the spatial diffusion (K) and convection (V_c), and the energy transport (first- and second-order terms). The right-hand side (r.h.s.) corresponds to the primary, secondary and tertiary (only for antinuclei) source terms, and the sink (spallative destruction) for the considered species. The most general form for the diffusion coefficient is $K(E, \vec{r})$. Energy gain and losses depend on $(E, \vec{r})$ as well. The first-order term $f_{\rm o}(E, \vec{r})$ corresponds to the sum of four contributions: ionization, Coulomb and adiabatic losses, and first-order reacceleration. Ionization losses take place in the neutral interstellar medium (ISM) (90% H and 10% He), while the Coulomb losses take place in the completely ionized plasma, dominated by the scattering of the thermal electrons, for which we take an average density of $\langle n_e\rangle = 0.033\ \mathrm{cm}^{-3}$ and a temperature of $T_e = 10^4$ K. Complete formulae for these two effects are compiled, for example, in Refs. [10,11]. The spatial dependence of these two terms is encoded in the distribution of the neutral and ionized gas. Adiabatic losses are due to the expanding wind and their spatial dependence is related to the gradient of $\vec{V}_c$. The last contribution to $f_{\rm o}(E, \vec{r})$ has the same origin as the second-order term $s_{\rm o}(E, \vec{r})$. Those come from the scattering of the charged particles off the turbulent magnetic fields of the Galaxy. As well as being responsible for spatial diffusion, the Alfvénic waves also lead to energy drift and reacceleration. A minimal reacceleration scheme is well motivated [12] and allows us to calculate the f_o and s_o coefficients. Similar, albeit more empirical forms, have also been used [13,14]. In all these models, the strength of the reacceleration is mediated via the Alfvénic speed V_a of the scatterers.

A. The two-zone disk-halo model

A full numerical treatment is generally required to solve the transport equation, as described, e.g., in [15]. However, analytical (or semianalytical) solutions may be derived assuming a simplified description of the spatial dependence of some parameters in Eq. (1). The two-zone diffusion model [16,17], based on the description of the Galaxy as a thin gaseous disk embedded in a thick diffusive halo, proved to be successful in reproducing the nuclear [14,18,19], antiproton [20] and radioactive isotopes data [19]. It also allows us to treat contributions from dark matter (or other exotic) sources located in the diffusive halo [21–23], which is the aim of this paper. Next, we summarize the salient features of this model, which has been extensively detailed in Refs. [14,24,25].

(a) *Geometry* (L, R *and* h). The Galaxy is defined as a cylinder with a diffusive halo of half-height $z = L$ and radius $r = R$. The halo thickness L is a free parameter of the model. The interstellar (IS) gas and the nuclei accelerators are contained in a thin disk of half-height $h \ll L$. The two parameters h and R are set to 100 pc and 20 kpc, respectively.

(b) *Diffusion coefficient* (K_0 *and* δ). Diffusion arises because charged particles interact with the galactic magnetic field inhomogeneities. The diffusion coefficient $K(\vec{r}, E)$ is related to the power spectrum of these inhomogeneities, which is poorly known. Several analytical forms for K have been assumed in the literature. We consider here the standard rigidity ($\mathcal{R} = pc/Ze$) dependent form $K(E) = \beta K_0 \times \mathcal{R}^\delta$, where the normalization K_0 is expressed in units of $\mathrm{kpc}^2\ \mathrm{Myr}^{-1}$. The same diffusion coefficient is assumed throughout the Galaxy, i.e. in the disk and in the halo. K_0 and δ are free parameters of the model.

(c) *Galactic wind and Alfvénic speed* (V_c *and* V_a). The convective wind is assumed to be of a constant magnitude directed outwards perpendicular to the galactic plane $\vec{V}_c = V_c\vec{e}_z$. The reacceleration strength, mediated by the Alfvén velocity V_a, is confined to the thin disk. The first- and second-order terms $f_{\rm o}$ and $s_{\rm o}$ in Eq. (1) follow the formulation given in Ref. [14].

The free parameters of this propagation model—the diffusive halo size L, the normalization K_0 and the slope δ of the diffusion coefficient, the value of the constant galactic wind V_c and the level of reacceleration through the Alfvénic speed V_a—were constrained from the study of the B/C ratio in Refs. [14,24]. In this paper, we take advantage of the parameters found in Ref. [14] and listed in Table I. Actually, when fitting to existing B/C data, a strong degeneracy of the transport parameters is observed, meaning that many sets of these five parameters are acceptable and lead to the same B/C ratio, but also to the same secondary (standard) antiproton flux [20]. This degeneracy is broken

TABLE I. Transport parameters providing the maximal, median and minimal primary antideuteron flux and compatible with B/C analysis ($\chi^2_{\mathrm{B/C}} < 40$) [14,24].

Case	δ	K_0 (kpc^2/Myr	L (kpc)	V_c (km/s)	V_A (km/s)	$\chi^2_{\mathrm{B/C}}$
max	0.46	0.0765	15	5	117.6	39.98
med	0.70	0.0112	4	12	52.9	25.68
min	0.85	0.0016	1	13.5	22.4	39.02

for sources located in the diffusive halo, leading to large astrophysical uncertainties for the relevant fluxes [21,26,27]. The same conclusions are obtained here for antideuterons. We will come back to this point in Secs. IV and V.

B. The case of antideuterons

Once the astrophysical framework for the transport of (anti)nuclei is set, the calculation of the antideuteron flux rests on the $\bar{d}$ specificities regarding the source term and its nuclear interactions [r.h.s. of Eq. (1)]. The source term for antinuclei is usually cast in separate contributions:

$$Q_{\mathrm{source}}(\vec{r}, E) = Q_{\mathrm{prim}}(\vec{r}, E) + Q_{\mathrm{sec}}(\vec{r}, E) + Q_{\mathrm{ter}}(\vec{r}, E). \quad (2)$$

Among these three terms, only the primary and secondary are *true* sources. They will be discussed in Secs. IV and V.

The tertiary term was emphasized in Ref. [28] to describe the process corresponding to the nonannihilating interaction of a CR antinucleus with an atom of the IS gas. In a medium of constant density n (v is the CR velocity):

$$Q_{\mathrm{ter}}(\vec{r}, E) = \int_E^{+\infty} n v' \frac{d\sigma^{\mathrm{non\text{-}ann}}_{\bar{d}H\to\bar{d}X}}{dE}\{E' \to E\} N(\vec{r}, E') dE' - n v \sigma^{\mathrm{non\text{-}ann}}_{\bar{d}H\to\bar{d}X}\{E\} N(\vec{r}, E). \quad (3)$$

The cross sections in Eq. (3) refer to inelastic nonannihilating processes and are detailed in the Appendix. The tertiary mechanism does not actually create new antideuterons. It merely states that the number of antinuclei observed at energy E has to take into account the redistribution of those with energy $E' > E$ (first term, positive contribution), minus the total number of $\bar{d}$ redistributed to lower energies (second term, negative contribution). The tertiary contribution is treated as a corrective factor and dealt with iteratively: the equilibrium spectrum $N^{(0)}(\vec{r}, E)$ is first calculated with $Q^{(0)}_{\mathrm{ter}} \equiv 0$, then $Q^{(1)}_{\mathrm{ter}}$ is calculated with $N^{(0)}(\vec{r}, E)$ in Eq. (3) to obtain $N^{(1)}(\vec{r}, E)$, etc. For antideuterons, due to the small cross section—as shown in Ref. [8]—only one iteration is necessary to converge to the solution (compared to a few iterations for antiprotons [20]).

Hence, whether secondary or primary (or a mixture of both) sources are considered, three cross sections always enter the calculation: the differential nonannihilating inelastic cross section $d\sigma^{\mathrm{non\text{-}ann}}/dE$, the total nonannihilating inelastic cross section $\sigma^{\mathrm{non\text{-}ann}}$ and the total annihilating inelastic cross section σ^{ann} [appearing in the r.h.s. of Eq. (1)]. Considering the ISM as a mixture of H and He, the full calculation requires six cross sections. Our calculations, based on the parameterizations discussed at length in Duperray *et al.* [8], are discussed in the Appendix where, in particular, we update $d\sigma^{\mathrm{non\text{-}ann}}/dE$. Note however, that even if some of these cross sections are slightly modified, the impact on the propagated spectra does not change the conclusions found in Ref. [8].

In the two-zone diffusion/convection/reacceleration model, it is possible to extract semianalytical solutions of Eq. (1), based on Bessel expansions of the transport equation. We do not wish to repeat the various steps of this derivation, nor to rewrite the complete form of the solutions, which have already been given in several papers. The solution for the so-called antideuteron standard source (of secondary origin in the galactic disk) and the numerical procedure to treat reacceleration is detailed in Ref. [20]. The solution for an exotic source distributed in the whole diffusive halo of the Galaxy can be found in Refs. [21,26]. Actually these two papers refer to $\bar{p}$, but formally, the solutions apply to $\bar{d}$ as well.

III. ANTIDEUTERON PRODUCTION

The production of cosmic antideuterons is based on the fusion process of a $\bar{p}$ and $\bar{n}$ pair. One of the simplest but powerful treatments of the fusion of two or more nucleons is based on the so-called coalescence model which, despite its simplicity, is able to reproduce remarkably well the available data on light nuclei and antinuclei production in different kinds of collisions. In the coalescence model, the momentum distribution of the (anti)deuteron is proportional to the product of the (anti)proton and (anti)neutron momentum distribution [29,30]. That function depends on the difference $\Delta_{\vec{k}}$ between (anti)nucleon momenta. It is strongly peaked around $\Delta_{\vec{k}} \simeq \vec{0}$ (compare the minimum energy to form a $\bar{d}$, i.e. $4m_p$, with the binding energy ~2.2 MeV), so that

$$\vec{k}_{\bar{p}} \simeq \vec{k}_{\bar{n}} \simeq \frac{\vec{k}_{\bar{d}}}{2}. \quad (4)$$

The $\bar{d}$ density in momentum space is thus written as the $\bar{p}$ density times the probability to find an $\bar{n}$ within a sphere of radius p_0 around $\vec{k}_{\bar{p}}$ (see, e.g., Ref. [31]):

$$\gamma \frac{d\mathcal{N}_{\bar{d}}}{d\vec{k}_{\bar{d}}} = \frac{4\pi}{3} p_0^3 \cdot \gamma \frac{d\mathcal{N}_{\bar{\mathrm{p}}}}{d\vec{k}_{\bar{p}}} \cdot \gamma \frac{d\mathcal{N}_{\bar{\mathrm{n}}}}{d\vec{k}_{\bar{n}}}. \tag{5}$$

The coalescence momentum p_0 is a free parameter constrained by data on hadronic production. Note that the coalescence model has been refined to account for heavy nuclei reactions (see, e.g., [32,33]), but as it is not relevant for this study, we will stick to the simple Eq. (5).

The number $d\mathcal{N}_{\mathrm{X}}^{\mathrm{R}}$ of particles X produced in a single reaction R and which momenta are $\vec{\mathrm{k}}_{\mathrm{X}}$ can be expressed as a function of the total available energy $\sqrt{s}$, the inclusive (i.e. total inelastic or reaction cross section) and the differential cross section:

$$d\mathcal{N}_{\mathrm{X}}^{R} = \frac{1}{\sigma_{\mathrm{inel}}^{\mathrm{R}}} d^3\sigma_{\mathrm{X}}(\sqrt{s}, \vec{\mathrm{k}}_{\mathrm{X}}). \tag{6}$$

For instance, in our specific case X are the antinucleons and antideuterons created in the pp, pHe and HeHe reactions between p-He CRs and H-He in the ISM. Assuming the usual equality between the unmeasured $\bar{n}$ and the measured $\bar{p}$ cross sections, and combining the two previous expressions Eqs. (5) and (6) we get

$$E_{\bar{d}} \frac{d^3\sigma_{\bar{d}}^{\mathrm{R}}}{d\vec{k}_{\bar{d}}} = \frac{1}{\sigma_{\mathrm{inel}}^{\mathrm{R}}} \cdot \frac{4\pi}{3} p_0^3 \cdot \frac{m_{\bar{d}}}{m_{\bar{p}}^2} \cdot \left(E_{\bar{p}} \frac{d\sigma_{\bar{\mathrm{p}}}^{\mathrm{R}}}{d\vec{k}_{\bar{p}}} \right)^2. \tag{7}$$

The hypothesis of factorization of the probabilities is fairly well established from experiments at high energies (see, e.g., [8]). For spallation reactions, however, the bulk of the antiproton production takes place for an energy $\sqrt{s} \sim 10$ GeV, which turns out to be of the same order of magnitude as the antideuteron mass. Pure factorization should break in that case as a result of energy conservation. Two ansatz have been used in order to correct that effect for this regime: In Refs. [1,7] it was assumed that, while the first antinucleon is produced with $\sqrt{s}$, the center of mass energy available for the production of the second antinucleon is reduced by twice the energy carried away by the first antinucleon. Instead, in Duperray *et al.* [8] the threshold production was phenomenologically taken into account through an $A + 2$ phase space factor. The latter description seems more appropriate as, while preserving the correct asymptotic properties, it does not favor any mechanism for the pair production [34].

The coalescence momentum p_0 is linked to the measured coalescence factor $B_{A=2}$ (hereafter simply B_2):

$$B_2 \equiv \sigma_{\mathrm{inel}}^{\mathrm{R}} \cdot E_{\bar{d}} \frac{d^3\sigma_{\bar{d}}^{\mathrm{R}}}{d\vec{k}_{\bar{d}}} \cdot \left(E_{\bar{p}} \frac{d\sigma_{\bar{\mathrm{p}}}^{\mathrm{R}}}{d\vec{k}_{\bar{p}}} \right)^{-2}, \tag{8}$$

so that

$$p_0 = \left(\frac{1}{B_2} \cdot \frac{m_{\bar{d}}}{m_{\bar{p}}^2} \cdot \frac{4\pi}{3} \right)^{-1/3}. \tag{9}$$

The B_2 coefficient has been measured for proton-proton, proton-nucleus and heavy ion collisions (see a summary and references in Refs. [8,35]). More recently, several other channels have also been measured at high energy: photo-production [35], deep inelastic scattering production [36] and e^+e^- production at the Z [37] and $\Upsilon(1S)$ [38] resonances. The e^+e^- channel is of particular interest for the DM annihilation reactions.

A. Hadronic production

For the hadronic processes, the coalescence momentum can directly be fitted to data. However, different assumptions regarding the set of data to retain can lead to different values of p_0. Note that many recent data are available for $A + A$ systems, in addition to pp and pA reactions. However, the mechanisms at play in heavy ion collisions are not necessarily those of lighter systems (see, e.g., the discussion in Sec. II.A of Ref. [8] and the results of Ref. [39]), so these reactions are discarded in the rest of our analysis.

Chardonnet *et al.* [7] used pp data from Refs. [40–42] and pA collisions from Ref. [42] (see Fig. 1 in Ref. [7]) to derive a coalescence momentum $p_0 = 58$ MeV. Based on kinematical relevance of the measured reactions, these authors disfavored the pp data from Ref. [41], but underlined that a value $p_0 = 75$ MeV, compatible with their whole set of data, would merely provide twice as many antideuterons.

In Duperray *et al.* [8], a larger set of data is used, including many pA reactions (see their Table I and references therein). The approach is more sound since a χ^2 analysis on the momentum distribution of the fragments was performed, taking also into account the phase space. This leads to an estimate of $p_0 = 79$ MeV. Note that at variance with the choice of Chardonnet *et al.* [7], Duperray *et al.* discarded the data from Ref. [42] because they give a poor χ^2 value compared to all other data. It is thus not surprising that these authors end up with a value close to $p_0 = 75$ MeV quoted in Chardonnet *et al.* [7]. In the present paper, we take directly the cross sections derived in Duperray *et al.* [8] using the value $p_0 = 79$ MeV.

B. Weak production

At CERN LEP energies, (anti)deuteron production occurs through e^+e^- annihilations into $q\bar{q}$ pairs, a mechanism similar to the $\bar{d}$ production in DM annihilation reactions. Based on theoretical arguments, it has been argued [31] that the antideuteron yields in e^+e^- reactions should be smaller than in hadronic reactions. However, the ALEPH Collaboration [37] has found that this theoretical prediction (see Fig. 5 in ALEPH paper) underestimates their measured $\bar{d}$ inclusive cross section. They derive (see their Fig. 6) a value $B_2 = 3.3 \pm 0.4 \pm 0.1 \times 10^{-3}$ GeV^2 at the Z resonance, which translates into $p_0 = 71.8 \pm 3.6$ MeV, very close to the $p_0 = 79$ MeV derived for the hadronic production. Hence, in the remainder of the paper, the value of $p_0 = 79$ MeV will be retained for both the processes of hadronic and electroweak origin.

IV. SECONDARY ANTIDEUTERONS

Secondary antideuterons are produced in the galactic disk from the collisions of cosmic protons and helium nuclei over the ISM. We evaluate here the $\bar{d}$ propagated fluxes as well as the nuclear and propagation uncertainties, similarly to what was done for $\bar{p}$ in Ref. [20].

A. Median flux

The secondary $\bar{d}$ flux is the sum of the six contributions corresponding to p, He and $\bar{p}$ cosmic-ray fluxes impinging on H and He IS gas (other reactions are negligible [8]). The p and He fluxes were fitted on BESS [43] and AMS [44–46] high energy data with a power law spectrum (see details in Ref. [20]) $\Phi(\mathrm{T}) = \mathrm{N}(\mathrm{T}/\mathrm{GeV}/\mathrm{n})^{-\gamma}$. The best fit corresponds to $N_\mathrm{p} = 13249\ \mathrm{m}^{-2}\,\mathrm{s}^{-1}\,\mathrm{sr}^{-1}\,(\mathrm{GeV}/\mathrm{n})^{-1}$ and $\gamma_\mathrm{p} = 2.72$, and $N_\mathrm{He} = 721\ \mathrm{m}^{-2}\,\mathrm{s}^{-1}\,\mathrm{sr}^{-1}\,(\mathrm{GeV}/\mathrm{n})^{-1}$ and $\gamma_\mathrm{He} = 2.74$. The uncertainty on these two fluxes is small and leads to negligible uncertainties in the $\bar{p}$ and $\bar{d}$ spectrum. Contributions to the $\bar{d}$ flux from $\bar{p}$ + H and $\bar{p}$ + He reactions are evaluated using the $\bar{p}$ flux calculated in the same run. The production cross sections for these specific processes are those given in Ref. [8].

The different contributions to the total secondary antideuteron flux, calculated for the best-fit propagation configuration (the “med” one in Table I), i.e. $K_0 = 0.0112\ \mathrm{kpc}^2\,\mathrm{Myr}^{-1}$, $L = 4$ kpc, $V_c = 10.5\ \mathrm{km}\,\mathrm{s}^{-1}$ and $V_a = 52.1\ \mathrm{km}\,\mathrm{s}^{-1}$, are shown in Fig. 1. As expected, the dominant production channel is the one from $p - p$ collisions, followed by the one from cosmic protons on IS helium (p-He). As shown in Ref. [8], the $\bar{p}$ + H channel is dominant at low energies, and negligible beyond a few GeV/n. The effect of energy losses, reacceleration and tertiaries add up to replenish the low-energy tail. The maximum of the flux reaches the value of $2 \cdot 10^{-7}$ particles $(\mathrm{m}^2\,\mathrm{s}\,\mathrm{sr}\,\mathrm{GeV}/\mathrm{n})^{-1}$ at 3–4 GeV/n. At 100 MeV/n it is decreased by an order of magnitude, thus preserving an interesting window for possible exotic contributions characterized by a flatter spectrum.

B. Propagation uncertainties

For a determination of the propagation uncertainties, we follow the same approach as in Ref. [20]. We calculate the secondary antideuteron flux for all the propagation parameter combinations providing an acceptable fit to stable nuclei [14]. The resulting envelope for the secondary antideuteron flux is presented in Fig. 2. The solid lines delimit the uncertainty band due to the degeneracy of the propagation parameters: at energies below 1–2 GeV/n, the uncertainty is 40–50% around the average flux, while at 10 GeV/n it decreases to ~15%. This behavior is analogous to that obtained for $\bar{p}$ [20] and is easily understood. The degenerate transport parameters combine to give the same grammage in order to reproduce the B/C ratio. Indeed, the grammage crossed by C to produce the secondary species B is also crossed by p and He to produce the secondary $\bar{p}$ and $\bar{d}$. In short, a similar propagation history associated with a well constrained B/C ratio explains the small uncertainty. With better measurement of B/C expected soon, e.g., from PAMELA [47] or TRACER [48], this uncertainty will further decrease and could become negligible.

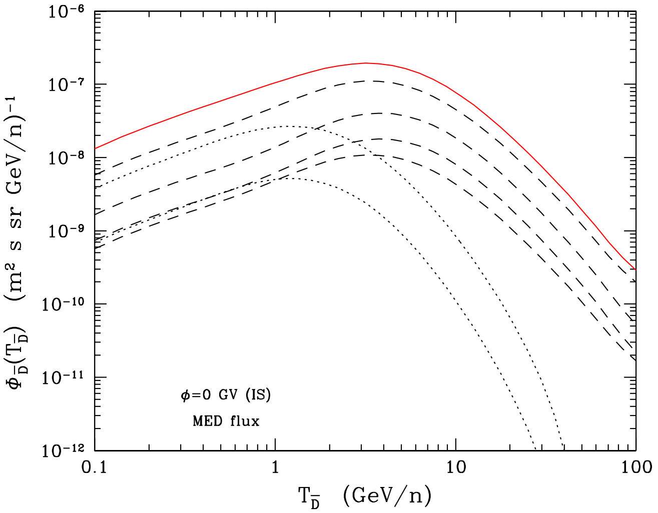

FIG. 1 (color online). Contribution of all nuclear channels to the $\bar{d}$ secondary flux. Dashed lines, from top to bottom refer to p + H, p + He, He + H, He + He. Dotted lines, from top to bottom stand for $\bar{p}$ + H, $\bar{p}$ + He. The solid line stands for the sum of all the components.

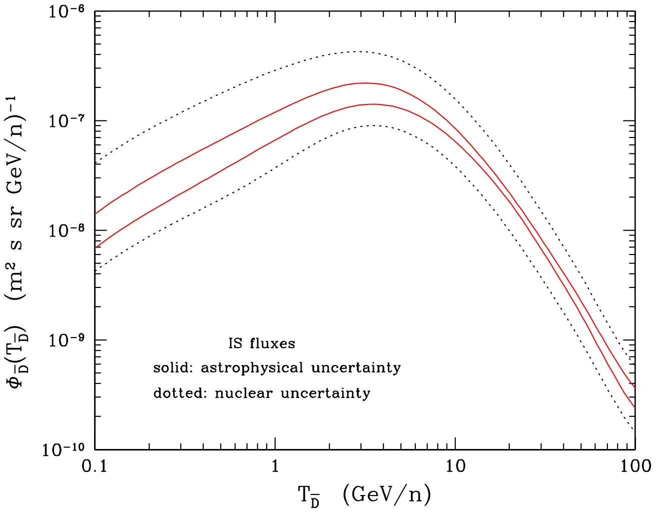

FIG. 2 (color online). Dominant uncertainties on the interstellar secondary $\bar{d}$ flux. Solid lines refer to the propagation uncertainty band. Dotted lines refer to the nuclear uncertainty band.

C. Nuclear uncertainty

The possible nuclear uncertainty can arise from two different sources. The first one is directly related to the elementary production process $d\sigma_{\bar{\mathrm{p}}}^{\mathrm{R}}$. It was found in Ref. [20] that this may be cast into a ±25% in the $\bar{p}$ propagated flux, so that it should be translated to a rough ±50% in the $\bar{d}$ flux. Second, there is the uncertainty on the coalescence momentum p_0. Using an independent model (i.e. different from the coalescence scheme) for $\bar{d}$ production, Ref. [8] found that, conservatively, the $\bar{d}$ background was certainly no more than twice the flux calculated with $p_0 = 79$ MeV.

To some extent, these two uncertainties are correlated as the value of p_0 depends on the choice for $d\sigma_{\bar{\mathrm{p}}}^{\mathrm{R}}$. Hence, to be very conservative and to keep a simple approach, we have spanned all hadronic production cross sections in the range $^{+100\%}_{-50\%}$ around their reference value. If we wished to translate this into an uncertainty on the coalescence momentum, this would lead to the *effective* range $p_0 = 79^{+26}_{-13}$ MeV. Finally, in order to estimate the maximal flux with the most conservative attitude (the higher the secondary flux, the lower the chance to outline an exotic contribution), the nonannihilating cross section was doubled, as its value is probably only a lower limit (see Appendix). On the other hand, to evaluate the minimal flux, we switched off the $\bar{p}$ + H(He) $\rightarrow \bar{d} + X$ contributions, which intensity remains very uncertain.

The dotted lines in Fig. 2 take into account the sum of all the possible uncertainties of nuclear source, as described above. At the lowest energies the flux is uncertain by almost 1 order of magnitude, at 100 GeV/n by a factor of 4. We have checked that the solar wind mildly decreases the IS flux at low energies but leaves the uncertainty magnitude unchanged. It is obvious from Fig. 2 that the uncertainties on nuclear and hadronic cross sections (dashed lines) are more important than the ones coming from the propagation models (solid lines). We emphasize once more our conservative attitude in estimating the nuclear band. However, if no dedicated campaigns of measurements for these cross sections will be carried out in the future, these uncertainties are not likely to be significantly reduced.

V. PRIMARY ANTIDEUTERONS

The source term for primary $\bar{d}$ to be cast into Eq. (1) is

$$q_{\bar{d}}^{\mathrm{prim}}(r, z, E) = \eta \xi^2 \langle \sigma_{\mathrm{ann}} v \rangle_0 \frac{dN_{\bar{d}}}{dE_{\bar{d}}} \left(\frac{\rho_{\mathrm{DM}}(r, z)}{m_\chi} \right)^2, \quad (10)$$

where $\langle \sigma_{\mathrm{ann}} v \rangle_0$ is the thermal average of annihilation cross section times the weakly interactive massive particle (WIMP) velocity, $dN_{\bar{d}}/dE_{\bar{d}}$ is the source spectrum, $\rho_{\mathrm{DM}}(r, z)$ is the distribution of the DM in the Galaxy and m_χ is the WIMP mass. The quantity $\langle \sigma_{\mathrm{ann}} v \rangle_0$ depends on the particle physics model. If not differently stated, we fix its value to $2.3 \cdot 10^{-26}\ \mathrm{cm}^3\,\mathrm{s}^{-1}$, which corresponds to a thermal cold dark matter (CDM) relic able to explain the observed amount of cosmological dark matter [49–51]. This will be our reference value for most of the analysis. The coefficient η depends on the particle being or not being self-conjugate: for instance, for a fermion it is 1/2 or 1/4 depending on whether the WIMP is a Majorana or a Dirac particle. In the following we will adopt $\eta = 1/2$. The quantity ξ parameterizes the fact that the dark halo may not be totally made of the species under scrutiny (e.g., a neutralino or a sneutrino) when this candidate possesses a relic abundance which does not allow it to be the dominant DM component (see, e.g., [52] or [53]). In this case $\rho_\chi = \xi \rho_{\mathrm{DM}}$ with $\xi < 1$. For our reference value for $\langle \sigma_{\mathrm{ann}} v \rangle_0$ clearly one has $\xi = 1$. The DM candidate may then be identified with a neutralino [21] or a sneutrino [54] in various supersymmetric schemes, but for the purposes of our discussion it does not need to be specified. We in fact wish to maintain the discussion at the most general level: we just need to specify the final-state particles produced in the DM annihilation process and the ensuing energy spectra. The final-state particles all belong to the standard model, and this allows us to perform our discussion on a totally general basis. We will at the end specify our candidate to be the neutralino and discuss experimental capabilities in the framework of some specific supersymmetric scheme.

Below, we briefly recall the main steps for the calculation of the source term, before focusing on the propagation of these antideuterons in the Galaxy (Sec. V C), which is one of the main novelties in this paper.

A. Antideuteron source spectrum

The production of antideuterons from the pair annihilation of dark matter particles in the halo of our Galaxy was proposed in [1]. The interest in this possible DM detection channel has been the physics case for the proposal of the GAPS experiment [2–4] and it has also been considered in Refs. [55–57].

As previously discussed (see Sec. III) the production of a $\bar{d}$ relies on the availability of a $\bar{p} - \bar{n}$ pair in a single DM annihilation. In the case of a WIMP pair annihilation, the differential multiplicity for antiproton production may be expressed as

$$\frac{dN_{\bar{p}}}{dE_{\bar{p}}} = \sum_{\mathrm{F,h}} B_{\chi \mathrm{h}}^{(\mathrm{F})} \frac{dN_{\bar{p}}^{\mathrm{h}}}{dE_{\bar{p}}}. \quad (11)$$

The annihilation into a quark or a gluon h is realized through the various final states F with branching ratios $B_{\chi\mathrm{h}}^{(\mathrm{F})}$. Quarks or gluons may in fact be directly produced when a WIMP pair annihilates or they may alternatively result from the intermediate production of Higgs bosons or gauge bosons. Each quark or gluon h then generates jets whose subsequent fragmentation and hadronization yield an antiproton energy spectrum $dN^{\rm h}_{\bar p}/dE_{\bar p}$. These spectra have been calculated by using a Monte Carlo simulation with the PYTHIA package [58], as discussed in Ref. [21].

As in Ref. [1], we assume that the probability to form an antiproton (or an antineutron) with momentum $\vec{k}_{\bar p}$ ($\vec{k}_{\bar n}$), is essentially isotropic:

$$\frac{dN_{\bar p}}{dE_{\bar p}}(\chi + \chi \to \bar p + \ldots) = 4\pi k_{\bar p} E_{\bar p} \mathcal{F}_{\bar p}(\sqrt{s} = 2m, E_{\bar p}). \tag{12}$$

Applying the factorization-coalescence scheme discussed above leads to the antideuteron differential multiplicity

$$\frac{dN_{\bar d}}{dE_{\bar d}} = \left(\frac{4p_0^3}{3k_{\bar d}}\right)\cdot\left(\frac{m_{\bar d}}{m_{\bar p}^2}\right)\cdot\sum_{\rm F,h} B^{\rm (F)}_{\chi \rm h}\left\{\frac{dN^{\rm h}_{\bar p}}{dE_{\bar p}}\left(E_{\bar p} = \frac{E_{\bar d}}{2}\right)\right\}^2. \tag{13}$$

We assume, as discussed in Sec. III, that the same value of the coalescence momentum $p_0 = 79$ MeV holds as for hadronic reactions.

The evaluation of the differential antiproton spectrum $dN^{\rm h}_{\bar p}/dE_{\bar p}$ follows the treatment of Ref. [21]. We refer to this paper for the details of the $\bar p$ spectra from all the annihilation channels. The resulting $\bar d$ source spectra from different final states are not directly shown here. Instead, we will provide examples of propagated $\bar d$ spectra for the various final states in Fig. 3.

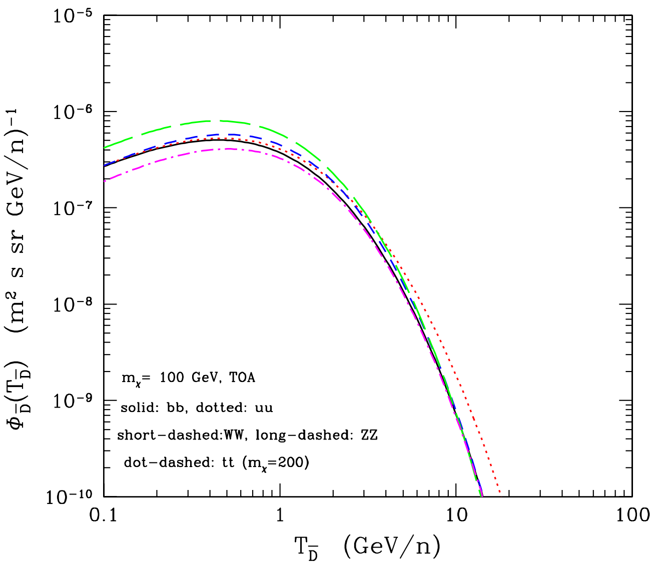

FIG. 3 (color online). Antideuteron flux for a WIMP mass $m_\chi = 100$ GeV annihilating into different final states: solid (black) line refers to $\bar b b$, dotted (red) line to $\bar u u$, short-dashed (blue) line to WW, long-dashed (green) line to ZZ. The dot-dashed (magenta) line refers to $\bar t t$ and $m_\chi = 200$ GeV. The annihilation cross section (here and in the following figures) is fixed at the value $\langle\sigma_{\rm ann} v\rangle_0 = 2.3\cdot 10^{-26}$ cm^3 s^{-1}.

B. Dark matter halo profile

The distribution of DM inside galaxies is a very debated issue (see, e.g., Ref. [59] for a brief highlight on recent results and relevant references). Different analyses of rotational curves observed for several types of galaxies strongly favor a cored dark matter distribution, flattened towards the central regions (Ref. [60] and references therein). On the other side, many collisionless cosmological N-body simulations in Λ-CDM models are now in good agreement among themselves [61], but for the very central regions some resolution issues remain open. It has been recently stressed that asymptotic slopes may not be reached at all at small scales [62–66]. However, it is not clear whether the central cusp is steepened or flattened when the baryonic distribution is taken into account (e.g., [67,68]). For definiteness, we consider a generic dark matter distribution:

$$\rho_\chi \equiv \rho_{\rm CDM}(r) = \rho_\odot\left\{\frac{r_\odot}{r}\right\}^\gamma\left\{\frac{1 + (r_\odot/a)^\alpha}{1 + (r/a)^\alpha}\right\}^{(\beta-\gamma)/\alpha}, \tag{14}$$

where $r_\odot = 8$ kpc is the distance of the Solar System from the galactic center. The spherical pseudo-isothermal and cored DM profile with $(\alpha, \beta, \gamma) = (2, 2, 0)$ will be the reference in our calculations. The total local—Solar System—CDM density has been set equal to $\rho_\odot = 0.42$ GeV cm^{-3}, the core radius to $a = 4$ kpc. This value and the total local density may be varied in large intervals by maintaining good agreement with observations. The antideuteron flux is very sensitive to the local distribution of dark matter $\rho_\odot$, since it appears squared in the determination of the flux, while it is less sensitive to the chosen dark matter distribution function (as was already underlined in Ref. [21] for $\bar p$). For completeness and for comparison, we also consider some of the profiles obtained from Λ-CDM simulations: (i) a standard Navarro, Frenk and White (NFW) profile having $(\alpha, \beta, \gamma) = (1, 3, 1)$, with $a = 21.746$ kpc [69], (ii) the steeper DMS-1.2 (1,3,1.2) profile with $a = 32.62$ kpc [70], (iii) and the modified NFW profile with a logarithmic slope (hereafter N04), with $a = 26.4$ kpc [62] (similar to the Einasto profile [64]). Scale radii for NFW and DMS-1.2 profiles are taken from Ref. [71], while the parameters for the N04 DM density distribution are the same as in Ref. [72]. All these profiles are normalized to $\rho_\odot = 0.42$ GeV cm^{-3}, in order to isolate the effect of the local density, which can be easily rescaled in the flux evaluation. We do not include any boost factor due to halo substructures. This conservative attitude is corroborated by the results of Lavalle *et al.* [59], where it has been shown that the boost factor is typically close to unity: only for some extreme and unlikely configuration can it reach a factor of 10.

C. Primary antideuteron flux and uncertainties

In the present section, we show our results for the propagated antideuteron flux from DM annihilation. We follow the prescriptions detailed in the previous sections for the production and the propagation of antideuterons. Top-of-atmosphere (TOA) fluxes are derived from the IS ones treating the effect of the solar modulation with the force field approximation. If not differently stated, TOA fluxes correspond to a solar minimum activity with modulation potential $\phi = 0.5$ GV. For the reference propagation configurations, we refer the reader to Table I.

1. Fluxes for various annihilation states

Figure 3 displays the $\bar{d}$ flux from a WIMP of mass $m_\chi = 100$ GeV. Each curve corresponds to different pure (*i.e.* with BR = 1) annihilation final states: $\bar{b}b$, $\bar{u}u$, WW, ZZ and $\bar{t}t$ (for which $m_\chi = 200$ GeV). The aim of the figure is to show the effect on the observable flux of the different $\chi - \chi$ annihilation final states from which the $\bar{d}$ originate. The transport parameters are the med ones of Table I (providing the best fit to B/C data) and the fluxes are not modulated (IS spectra). In the low-energy part of the spectrum—around and below 1 GeV/n—it turns out that these fluxes show quite similar shapes and comparable normalization when varying the final state. This energetic range is the one in which a primary flux might emerge from the secondary counterpart. In addition, as we will also discuss at the end of our paper, it is the window explorable by experiments in a near future. For these reasons, we will adopt the antideuteron yield from an annihilation into a pure $\bar{b}b$ final state as a simple but representative case for our discussions.

2. Propagation uncertainties

Figure 4 shows the uncertainties on the primary $\bar{d}$ flux due to propagation parameters. The three curves (dashed line: IS fluxes; solid lines: TOA fluxes) correspond to the maximum, median and minimal set of propagation parameters as gathered in Table I. The band between the upper and lower curve estimates the uncertainty due to propagation. At the lowest energies of hundreds of MeV/n the total uncertainty reaches almost 2 orders of magnitude, while at energies above 1 GeV/n it is about a factor of 30. The figure refers to a WIMP mass of 50 GeV but the results are insensitive to this parameter, as well as from the solar modulation. The magnitude of the propagation uncertainty is similar to the one affecting the primary antiprotons [21], as explained in Fig. 5. This behavior is drastically different from that observed on the secondaries (see Fig. 2). Indeed, their propagation history is very different. Whereas secondaries originate from standard sources in the thin disk of the Galaxy, exotic primaries are produced in all the diffusive halo of the Galaxy. As shown in Ref. [73], these primary antinuclei do not suffer large energy losses, reacceleration or tertiary redistribution as they rarely cross the thin disk. Most of them arrive at Earth—substantially unshifted in energy—from an effective diffusion cylinder of height $L^* = \min(L, 2K/V_c)$ and radius of a few L^* centered on the observer [74]. Hence, the parameters driving the uncertainty on the primaries are, at high energy, the range allowed for the halo size L (see Table I); whereas, at lower energy, this uncertainty is further increased by the

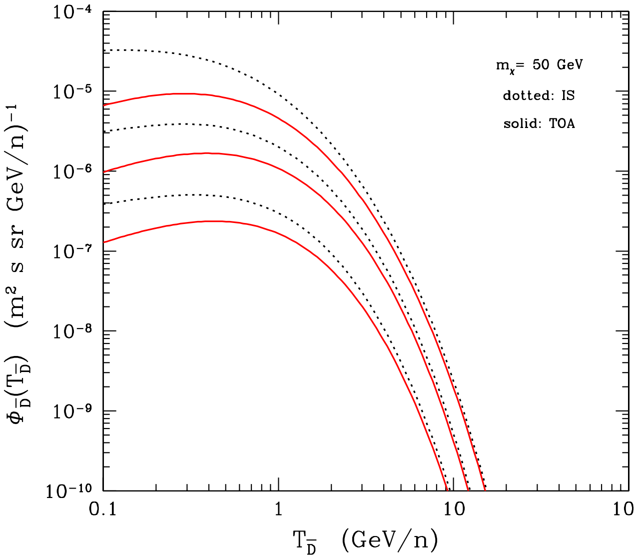

FIG. 4 (color online). Antideuteron flux for WIMPs of $m_\chi = 50$ GeV. Dotted (black) lines refer to the interstellar flux. Solid (red) lines stand for the top-of-atmosphere flux, modulated at solar minimum. For each set of curves, the three lines refer to the maximal, median and minimal propagation configurations defined in Table I.

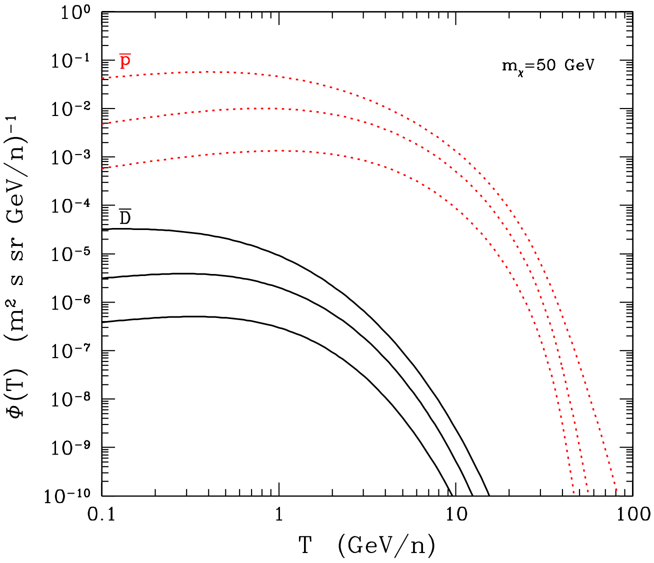

FIG. 5 (color online). Uncertainty due to propagation models on the antideuteron (black solid lines) and antiproton (red dotted lines) interstellar fluxes. The WIMP mass has been fixed at the value $m_\chi = 50$ GeV. For each set of curves, the three lines refer to the maximal, median and minimal propagation configurations defined in Table I.

effect of the galactic wind ($2K/V_c$ becomes smaller than L).

When comparing in details the $\bar{p}$ and the $\bar{d}$ fluxes from Fig. 5, the following conclusions can be drawn. First, the antiproton fluxes are a factor of 10^4 higher than the antideuteron ones, as expected from the fusion process into $\bar{d}$. Then, at high energies the difference between the two fluxes is to be ascribed to their source spectra, which for antideuterons is the square of the antiproton one. This effect, added to the different weight of destruction cross sections, is visible also in the lower energy tail of the spectrum. The destruction of the antideuteron nuclei on the ISM alters the flux by a factor of 2, while the antiproton one is modified by a mere 20–25%.

3. Dark matter halo profile uncertainty

The effect of changing the DM distribution function $\rho_{\rm DM}(r, z)$ on the $\bar{d}$ flux is demonstrated in Fig. 6. We only modify the shape of the density distribution (as discussed in Sec. V B), while keeping frozen the local DM density to $\rho_\odot = 0.42\ {\rm GeV/cm^3}$. The DM mass is $m_\chi = 50\ {\rm GeV}$, but as explained in the previous section, the source term mostly factors out, so that these conclusions hold for any neutralino mass. We plot the ratio $(\phi_{\bar{d}} - \phi_{\bar{d}}^{\rm ref})/\phi_{\bar{d}}^{\rm ref}$ where $\phi_{\bar{d}}^{\rm ref}$ is the reference flux calculated with the cored isothermal profile and $\phi_{\bar{d}}$ corresponds to the NFW, DMS-1.2 and N04 profiles (see Sec. V B). The two classes of curves correspond to the maximal (upper, solid line) and median (lower, dotted line) propagation parameters. The difference on the fluxes calculated with the minimal set of propagation parameters (not shown) is negligible.

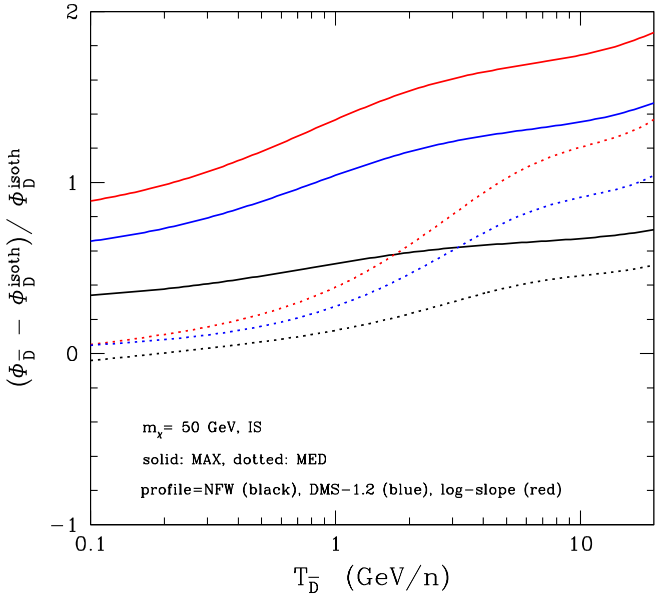

FIG. 6 (color online). Effect of changing the DM halo density profile, for a $m_\chi = 50$ GeV WIMP and for the max (solid line) and med (dotted line) configurations of Table I. The effect is shown as the relative change in the IS antideuteron flux as compared with the reference case of a cored isothermal profile. The lower (black) lines refer to the NFW profile [69], the median (blue) lines to a cuspy profile with 1.2 slope [70] and the upper (red) lines to the N04 profile of Ref. [62].

The increasing steepness of the profile in central regions of the Galaxy is responsible for an increase of the $\bar{d}$ flux which is more relevant for higher diffusive halos. In the case $L = 15$ kpc, the $\bar{d}$ obtained with a 1.2 cuspy profile [70] is a factor of 2 higher than the cored one, while the NFW [69] halo gives fluxes 30–40% higher than the isothermal one depending on energy. The highest flux is obtained with the log-slope NFW-like profile of Navarro *et al.* [62], which predicts, among the considered DM profiles, the highest DM density in a wide radial interval around the Solar System, although it is flatter than the DMS-1.2 and NFW profiles in the central kpc of the Galaxy. The flux obtained with the median parameters ($L = 4$ kpc) is less significantly modified by a change in the halo profile. Indeed, a charged particle produced around the galactic center can more easily reach the Solar System when the magnetic diffusive halo is larger and when it is more energetic.

VI. POTENTIAL FOR DETECTION: RESULTS AND DISCUSSION

We now turn to the determination of the total flux we can expect from the standard astrophysical source (see Sec. IV) added to a possible contribution from DM annihilation. In Fig. 7, we show the IS and TOA (solar minimum) secondary and primary $\bar{d}$ fluxes, and their sum. The primary flux is for a WIMP with mass $m_\chi = 50$ GeV, annihilation cross section $\langle\sigma_{\rm ann} v\rangle_0 = 2.3 \cdot 10^{-26}\ {\rm cm^3\,s^{-1}}$, an isothermal profile and $\rho_\odot = 0.42\ {\rm GeV/cm^3}$, as in the previous figures. The discrepancy between primary and secondary flux for $T_{\bar{d}} \lesssim 2$ GeV/n is striking. A signal from DM annihilation as the one in our example would definitely increase by a large amount the number of expected antideuterons in the lowest energy bins with respect to the purely secondary flux. At 100 MeV/n the expected $\bar{d}$ flux from a cosmologically dominant DM particle of 50 GeV mass is 2 orders of magnitude larger than the secondary $\bar{d}$ flux calculated within the same propagation model. One has to remind that the primary flux scales as m_χ^2: this means that, in the low-energy sector, the signal can overwhelm the background up to masses of the order of few hundreds of GeV. This figure demonstrates that the search for cosmic antideuterons is definitely one of the most powerful indirect detection means for the DM annihilation in the halo of our Galaxy. The discrimination power between signal and background can be as high as few orders of magnitude. A major limit to this kind of experimental inspection may reside in the tiny level of the expected flux (about 4 orders of magnitude less abundant than antiprotons), which never-

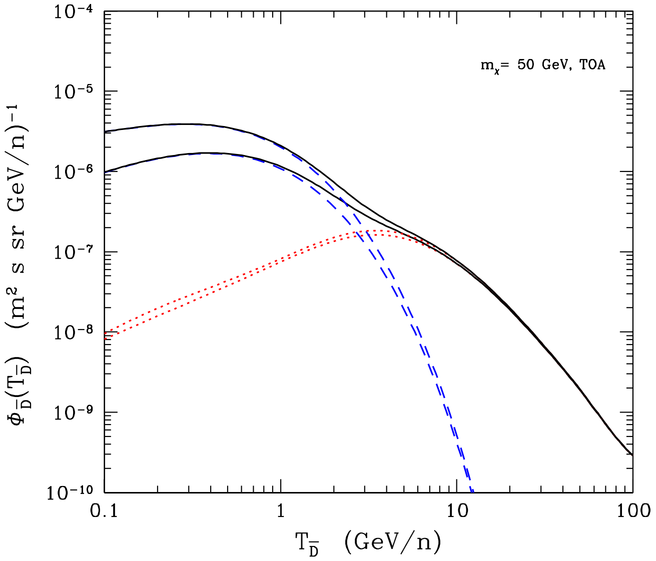

FIG. 7 (color online). Interstellar and top-of-atmosphere (TOA) antideuteron fluxes. The dashed (blue) line shows the primary flux for $m_\chi = 50$ GeV and $\langle\sigma_{\rm ann} v\rangle_0 = 2.3 \cdot 10^{-26}\ {\rm cm}^3\,{\rm s}^{-1}$, the dotted (red) line denotes the secondary component and the solid (black) line stands for the total (signal + background) flux. The propagation model is the median one in Table I.

theless is foreseen to become experimentally accessible in the near future [3,4,75,76].

Figure 8 displays the TOA $\bar{d}$ flux for the median propagation parameters and at solar minimum. Together with the secondary flux, we plot the primary one for three different WIMP masses: 50, 100, 500 GeV and for the same reference value of the annihilation cross section. As discussed above, lighter WIMPs would provide a striking signal, and sensitivity is present for masses up to few hundreds of GeVs.

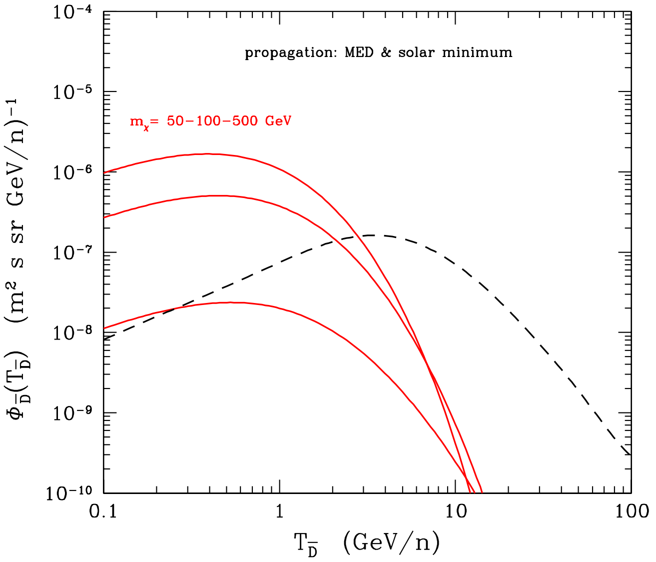

FIG. 8 (color online). TOA fluxes for primary (solid lines) and secondary (dashed line) antideuterons for the median propagation parameters. From top to bottom, the solid lines refer to WIMPs with mass $m_\chi = 50$, 100, 500 GeV.

The discrimination power between primary and secondary $\bar{d}$ flux may also be deduced from Fig. 9. The ratio of the primary to total TOA $\bar{d}$ flux is plotted as a function of the kinetic energy per nucleon, for the three representative propagation models and different WIMP masses (the annihilation cross section is again fixed at the reference value). This ratio keeps higher than 0.7 for $T_{\bar{d}} < 1$ GeV/n except for $m_\chi = 500$ GeV. For propagation models with $L \gtrsim 4$ kpc—which is a very reasonable expectation—this ratio is at least 0.9 for masses below 100 GeV. Increasing the WIMP mass, we must descend to lower energies in order to maximize the primary-to-secondary ratio. However, for a $m_\chi = 500$ GeV WIMP we still have a 50–60% of DM contribution in the 0.1–0.5 GeV/n range. Of course, the evaluation of the theoretical uncertainties presented in this paper must be kept in mind while confronting to real data. Figure 9 clearly states that the antideuteron indirect DM detection technique is probably the most powerful one for low and intermediate WIMP-mass haloes.

We finally discuss in Fig. 10 a possible experimental short term scenario. The secondary $\bar{d}$ flux for the median configuration of Table I is plotted alongside the primary flux from $m_\chi = 50$ GeV, calculated for the maximal, me-

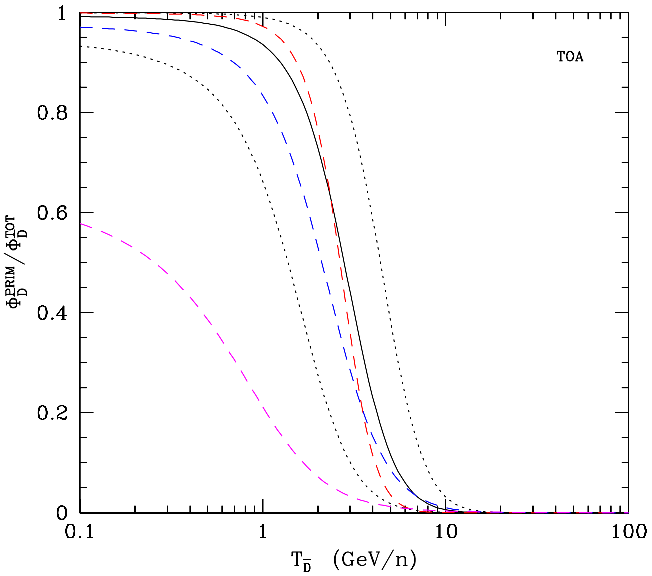

FIG. 9 (color online). Ratio of the primary to total (signal + background) TOA antideuteron flux. Solid (black) curve refers to a WIMP mass of $m_\chi = 50$ GeV and for the med propagation parameters. Dotted (black) lines show the max (upper) and min (lower) cases. Dashed lines refer to the med propagation parameters and different masses, which are (from top to bottom) $m_\chi = 10$, 100, 500 GeV (red, blue, and magenta, respectively).

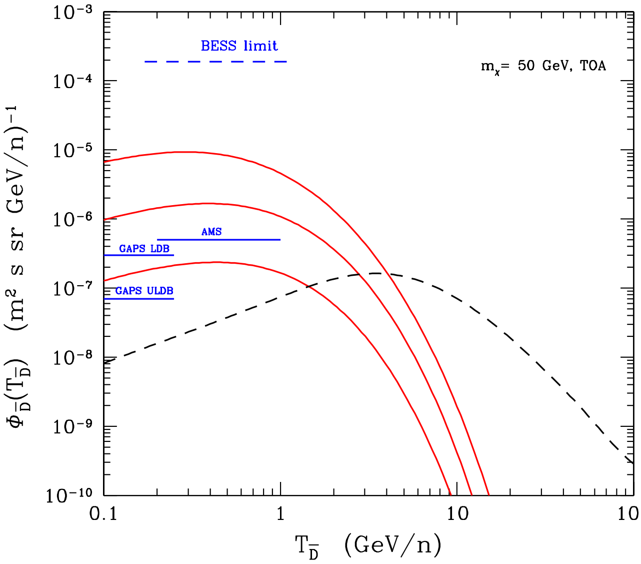

FIG. 10 (color online). TOA primary (red solid lines) and secondary (black dashed line) antideuteron fluxes, modulated at solar minimum. The signal is derived for a $m_\chi = 50$ GeV WIMP and for the three propagation models of Table I. The secondary flux is shown for the median propagation model. The upper dashed horizontal line shows the current BESS upper limit on the search for cosmic antideuterons. The three horizontal solid (blue) lines are the estimated sensitivities for (from top to bottom) AMS-02 [75], GAPS on a long (LDB) and ultralong (ULDB) duration balloon flights [3,4,76].

dian and minimal propagation scenarios. The present BESS upper limit on the (negative) antideuteron search [6] is at a level of $2 \cdot 10^{-4}$ $(\mathrm{m}^2\,\mathrm{s}\,\mathrm{sr}\,\mathrm{GeV/n})^{-1}$. We also plot the estimated sensitivities of the gaseous antiparticle spectrometer GAPS on a long duration balloon flight (LDB) and an ultralong duration balloon mission (ULDB) [3,4,76], and of AMS-02 for three years of data taking [75]. The perspectives to explore a part of the region where DM annihilation are mostly expected (i.e. the low-energy tail) are very promising. If one of these experiments will measure at least 1 antideuteron, it will be a clear signal of an exotic contribution to the cosmic antideuterons. Note that for AMS, a sensitivity at the level of the one at low energy should be obtained beyond 2.3 GeV/n thanks to the RICH [75,77]. This higher energy region would be complementary to a low-energy detection.

Prospects for antideuteron searches for specific dark matter candidates are shown in Figs. 11–13, where the expected capabilities of GAPS ULDB are confronted with theoretical predictions for neutralino dark matter in various supersymmetric schemes. The results are shown in terms of the effective annihilation cross section $\xi^2\langle\sigma_{\mathrm{ann}}v\rangle_0$ as a function of the neutralino mass. We recall that DM annihilation signals are proportional to the square of the relic-particle density profile ρ_χ (which is in turn proportional to the total DM density through the rescaling factor ξ defined in Sec. V), to the low-energy thermally-averaged annihilation cross section $\langle\sigma_{\mathrm{ann}}v\rangle_0$ and inversely proportional to the square of the WIMP-mass m_χ. It is therefore convenient to show our prediction in the plane $\xi^2\langle\sigma_{\mathrm{ann}}v\rangle_0 - m_\chi$. The solid, long-dashed and short-dashed lines in Fig. 11 denote our estimate for GAPS ULDB to measure 1, 10 and 100 events, respectively. The number of events has been obtained by using an acceptance × time for the GAPS detector in its whole energy range of 1.33×10^7 $\mathrm{m}^2\,\mathrm{sr}\,\mathrm{s}\,\mathrm{GeV/n}$ [78], for which no contribution to the antideuteron signal is expected from the secondary component. The quoted number of events therefore refers uniquely to the signal component. The transport parameters used in the determination of the antideuteron fluxes are those which provide the median flux and a minimum of activity for the Sun has been considered for the solar modulation. For definiteness, the event lines have been calculated for the case of a pure $b\bar{b}$ DM annihilation final state. Figure 3 shows that no major differences are present when different final states are considered: we therefore consider the lines of Fig. 11 as a good estimate of the

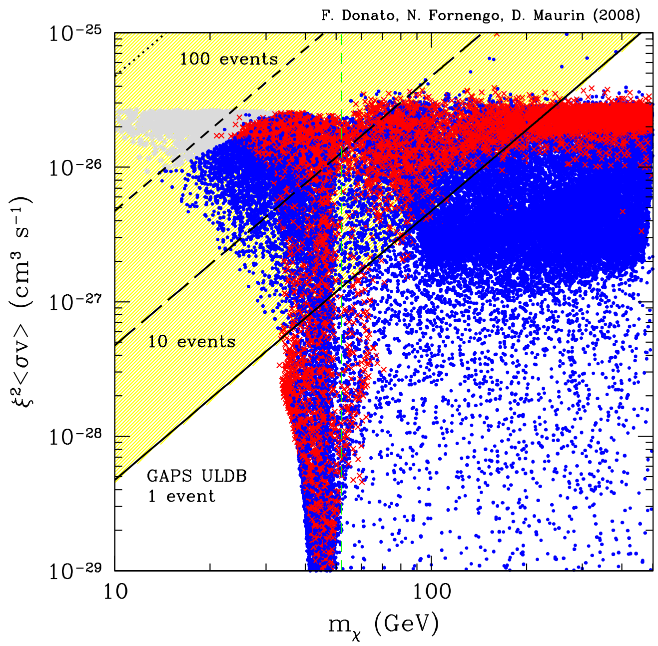

FIG. 11 (color online). GAPS ULDB reach compared to predictions for neutralino dark matter in low-energy supersymmetric models, shown in the plane effective annihilation cross section $\xi^2\langle\sigma_{\mathrm{ann}}v\rangle_0$ vs neutralino mass m_χ. The solid, long-dashed and short-dashed lines show our estimate for the capability of GAPS ULDB of measuring 1, 10 and 100 events, respectively, for the median propagation model of Table I. The scatter plot reports the quantity $\xi^2\langle\sigma_{\mathrm{ann}}v\rangle_0$ calculated in a low-energy MSSM (for masses above the vertical [green] dashed line) and in nonuniversal gaugino models which predict low-mass neutralinos [56,72,80–84]. (Red) Crosses refer to cosmologically dominant neutralinos, while (blue) dots stand for subdominant neutralinos. Gray points are excluded by antiproton searches.

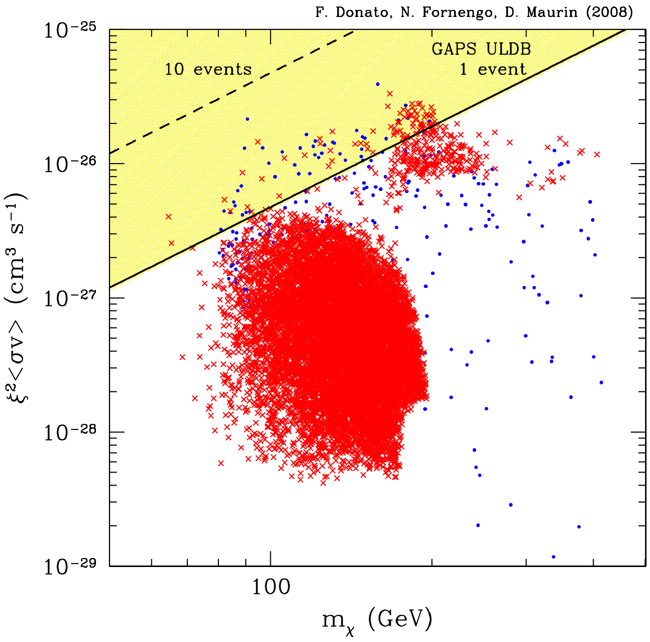

FIG. 12 (color online). The same as in Fig. 11, except that the supersymmetric predictions refer to a minimal SUGRA scheme.

GAPS ULDB sensitivity, to be confronted with theoretical predictions for specific candidates.

The scatter plot shows the distribution of points obtained in two supersymmetric models: for masses larger than about 50 GeV, the points refer to a low-energy minimal supersymmetric standard model (MSSM), where all the mass parameters are defined at the electroweak scale [21,79]. For masses lighter than 50 GeV, the scatter plots refer to the light-mass neutralinos in the models of Refs. [56,72,80–84] where the gaugino universality condition is violated. The (red) crosses denote configurations for which the relic neutralino is a dominant dark matter component (i.e. its calculated relic abundance falls in the WMAP range [49–51] for the CDM content of the Universe), while the (blue) points refer to subdominant neutralinos (for these points $\xi = \Omega_\chi h^2/(\Omega_{\rm CDM} h^2)_{\rm WMAP}$ applies). In the case of the standard MSSM, our prediction is that up to about a 20 events could be detected, for masses between 50 and 100 GeV. In the case of the low-mass neutralino models, a large number of events (up to a few hundreds of events for 10 GeV neutralinos) are expected for most of the relevant supersymmetric parameter space. In this situation, where the antideuteron fluxes are large, also antiproton production is expected to be sizeable. We therefore need to check that we do not produce an excess of exotic antiprotons which goes in conflict with current measurements on this antimatter channel. We employ here a $2-\sigma$ upper bound on the admissible excess of antiprotons over the background in the lowest energy bin of BESS [85,86] and AMS [87] of 0.68×10^{-2} m^{-2} sr^{-2} s^{-1} GeV^{-1}. These configurations, which exceed the antiproton bound [81], are shown by the gray points. We see that, once the $\bar{p}$ bound is included, up to about 100 $\bar{d}$ events are expected for neutralinos of 15–20 GeV. A detector like GAPS ULDB will therefore have a strong capability to access this class of supersymmetric models, which are currently only partially probed by antiprotons searches [81] and direct detection [88], depending on the actual galactic parameters, like profile and local density. In the case of the standard MSSM, GAPS ULDB

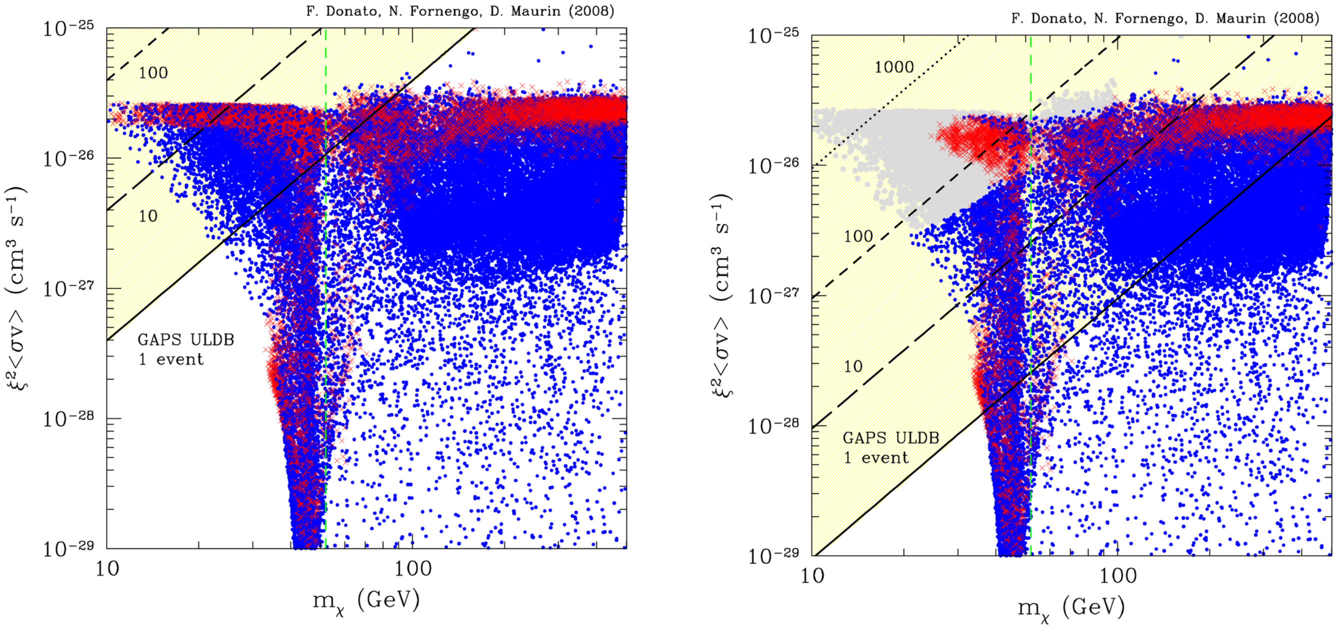

FIG. 13 (color online). The same as in Fig. 11, except that the astrophysical propagation parameters are those which predict minimal [(a) left panel] and maximal [(b) right panel] antideuteron fluxes. In the right panel, gray points are excluded by antiproton searches.

sensitivity allows us to probe neutralino masses up to 300 GeV.

The case of supersymmetric models endowed with supergravity (SUGRA) boundary conditions [89] are showed in Fig. 12 for the same astrophysical models of Fig. 11, together with our GAPS ULDB expectations. In the case of minimal SUGRA we predict up to a few events, for some specific supersymmetric configurations, although the bulk of the parameter space requires larger sensitivities to be probed.

The cases of the minimal and maximal set of transport parameters is shown in Fig. 13, again for the MSSM and gaugino nonuniversal models. In the case of the "min" set of parameters, light neutralinos may produce up to 70 events, while the in the standard MSSM at most a few events are predicted. For the "max" case we again are confronted with the fact that an excess of exotic antiprotons in conflict with current $\bar{p}$ measurements plays a role. Once this bound is properly taken into account, we obtain that 100–300 antideuterons are expected in the low/mid-mass range for neutralinos. Also in the standard MSSM model, up to 40 events are foreseen. In this case, the sensitivity of GAPS ULDB extends up to neutralino masses of the order of 500 GeV.

In conclusion, antideuteron searches offer very good opportunity of detecting a signal, for a variety of supersymmetric schemes. Especially low-mass neutralinos in gaugino nonuniversal models [56,72,80–84] provide expectations for a large number of events in a detector like GAPS ULDB, with good opportunities to clearly disentangle a signal.

VII. CONCLUSIONS

In this paper, we present a novel and updated calculation of both the secondary and primary antideuteron fluxes, with special attention to the determination of the uncertainties of nuclear and astrophysical origin which affect the theoretical predictions of the $\bar{d}$ flux. The galactic environment is treated in a two-zone diffusion model, the same that successfully reproduces cosmic-ray nuclear data, like, e.g., the boron-to-carbon ratio [14,24], and that is able to predict the observed antiproton flux [21]. We therefore refine our calculation of Ref. [1], where the antideuteron signal as a promising tool for dark matter searches was originally proposed.

We review the nuclear and astrophysical uncertainties and provide an up to date secondary (*i.e.* background) antideuteron flux. Propagation uncertainties for the secondary component range from 40–50 % around the average flux at energies below 1–2 GeV/n down to ~15% at 10 GeV/n. Nuclear uncertainties are largely dominant: a generous and conservative factor of 10 at very low energies, which reduces to a factor of 4 at 100 GeV/n.

The primary contribution has been calculated for generic WIMPs annihilating in the galactic halo, for the different production channels through which the antideuteron signal may be produced by DM annihilation. As for the antiproton [21] and positron signals [90], we obtain that the transport-related processes induce the largest source of uncertainty in the antideuteron flux: it ranges from a factor of 10 upward and downward with respect to the median, best-fit, prediction, in the low-energy range.

Our theoretical predictions have then been confronted with the expected sensitivities of future detectors, specifically GAPS [3,4,91] and AMS [5,75,87]. We have considered neutralinos as dark matter candidates and discussed three specific supersymmetric scenarios: a low-energy MSSM scheme, a gaugino nonuniversal supersymmetric model and a minimal SUGRA framework. For these classes of models we have analyzed the potentiality of the GAPS detector in a ultralong duration balloon flight and found that this detector will have the capabilities to detect up to a few hundred events for low-mass neutralinos (in the mass range from 10 to 50 GeV) in the gaugino nonuniversal models, and up to tens of events for 50–100 GeV neutralinos in standard low-energy MSSM. The sensitivity of GAPS ULDB on the neutralino mass extends up to 300–500 GeV in the low-energy MSSM.

In conclusion, antideuterons offer an exciting target for indirect dark matter detection for low and intermediate WIMP masses and future experiments will have a unique opportunity to clearly identify a signal.

ACKNOWLEDGMENTS

D. M. thanks R. Duperray for sharing the $\bar{d}$ cross section files, and R. Taillet and P. Salati for their help during several debugging sessions of the propagation code. We thank P. Salati for useful discussions and comments in the early stage of this study. We finally thank C. Hailey for providing us with information about the GAPS detector and F. Barao for the AMS detector. N. F. and F. D. acknowledge research grants funded jointly by the Italian Ministero dell'Istruzione, dell'Università e della Ricerca (MIUR), by the University of Torino and by the Istituto Nazionale di Fisica Nucleare (INFN) within the *Astroparticle Physics Project*.

APPENDIX A: CROSS SECTIONS

We review here the cross sections (total, elastic, inelastic and nonannihilating) used in the calculation for primary or secondary $\bar{d}$. Their detailed and thorough study, including the production, has been presented in Duperray *et al.* [8]. We do not repeat their arguments, but rather recall the main characteristics of these cross sections, providing alternative formulations, minor corrections or further checks when possible. However, none of these "updated" cross sections lead to significant changes in the calculation of the $\bar{d}$ flux, compared to that calculated with the cross sections presented in Ref. [8]. The main source of uncertainty remains the production cross section discussed in Sec. III.

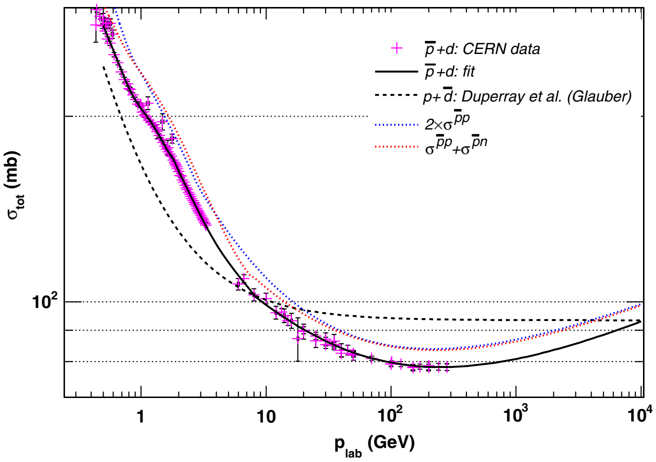

FIG. 14 (color online). Modeling of the total (elastic + inelastic) cross section $\sigma^{\mathrm{H}+\bar{d}}_{\mathrm{tot}}$. All curves are displayed as a function of the momentum. The black dashed line corresponds to the Glauber approximation used in Duperray *et al.* [8]. Crosses refer to data for the charge conjugate reaction $\bar{p}+d$ [93]. The black solid line is a crude fit of the latter reaction when data are available (the high energy regime comes from Ref. [93]). The two dotted curves illustrate a tentative estimate of $\sigma^{\bar{d}\mathrm{H}}$ as $2\sigma^{\bar{p}p}$ (blue) and $\sigma^{\bar{p}p}+\sigma^{\bar{p}n}$ (red), where we have modeled the latter cross sections by fits on the available data [93].

1. Total and elastic cross section

In Duperray *et al.* [8], the Glauber approximation was used. No data exist for the total cross section of the process $\bar{d}+\mathrm{H}$, but there are measurements for the charge conjugate reaction $d+\bar{p}$. Figure 14 shows various modeling of $\sigma^{\bar{d}p}_{\mathrm{tot}}$. Along with the charge conjugate measurements and the associated fit function, we also plot the Glauber cross section [8] and two modelings using $\bar{p}p$ and $\bar{p}n$ data. In this paper, we assume $\sigma^{\bar{d}p}_{\mathrm{tot}}=\sigma^{d\bar{p}}_{\mathrm{tot}}$, so that the total cross section is given by the black solid line of Fig. 14. Note that the combination $2\sigma^{\bar{p}p}$ and $\sigma^{\bar{p}p}+\sigma^{\bar{p}n}$ are very close to $\sigma^{d\bar{p}}$ data, overshooting it by a mere 10%.

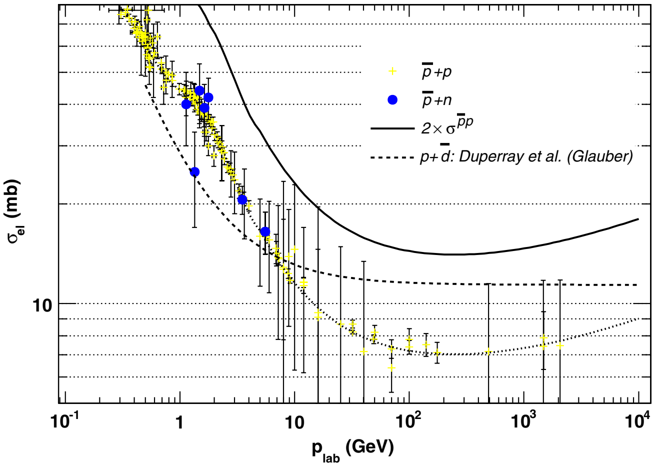

FIG. 15 (color online). Elastic cross sections as a function of the incident particle momentum. Yellow crosses and blue circles are CERN data [93] for $\bar{p}+p$ (the dotted line is a fit to these data) and $\bar{p}+n$ reactions. The elastic cross section $\sigma^{p\bar{d}}_{el}$ is modeled using $2\sigma^{\bar{p}p}_{el}$ (solid black line). The dash-dotted gray line corresponds to the Glauber cross section used in Duperray *et al.* [8]. See text for comments.

Concerning the elastic cross section, the situation is worse since no data exist even for the charge conjugate reaction. However, as seen in Fig. 14, the total cross section $\sigma^{d\bar{p}}$ is well approximated by $2\sigma^{\bar{p}p}$ or $\sigma^{\bar{p}p}+\sigma^{\bar{p}n}$, so this should also be the case for the elastic cross section. Since data for $\bar{p}n$ are scarce (Fig. 15, blue circles) as compared to those for $\bar{p}p$ (yellow crosses), we choose to approximate $\sigma^{p+\bar{d}}_{\mathrm{el}}\approx 2\sigma^{\bar{p}p}_{\mathrm{el}}$. This is shown on Fig. 15 as a black solid line, which is a factor of 2 larger than the Glauber description (black dashed line) used in Ref. [8].

2. Inelastic, total nonannihilating and differential redistribution cross sections

The inelastic cross section is simply obtained from

$$\sigma_{\mathrm{inel}}=\sigma_{\mathrm{tot}}-\sigma_{\mathrm{el}}, \tag{A1}$$

and is itself further expressed as

$$\sigma_{\mathrm{inel}}=\sigma^{\mathrm{non\text{-}ann}}_{\mathrm{inel}}+\sigma^{\mathrm{ann}}_{\mathrm{inel}}. \tag{A2}$$

The nonannihilating (non-ann) part corresponds to antideuterons that interact inelastically with H, but survive the collision, loosing a fraction of their initial energy.

In Ref. [1], the tertiary contribution was neglected, arguing that $\bar{d}$ (or symmetrically d) incident on a nucleon or on a nuclear target should have a small nonannihilating cross section owing of the small $\bar{d}$ (d) nuclear binding energy. As discussed in Ref. [8], this intuitive argument can be invalidated both on empirical evidence and on formal grounds (see discussion and references therein).

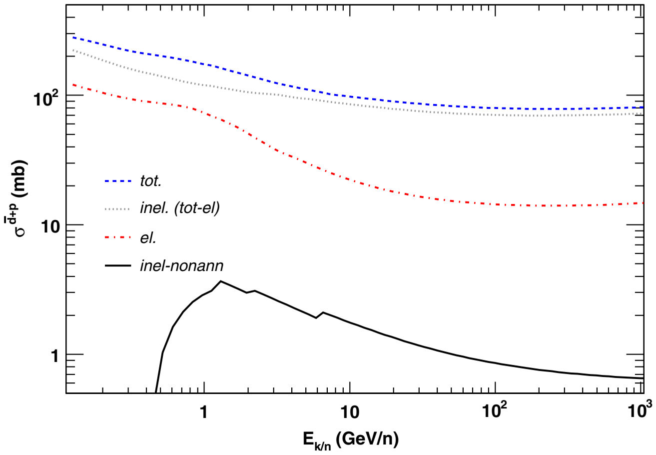

FIG. 16 (color online). From top to bottom: total, inelastic, elastic and inelastic nonannihilating cross sections for $\bar{d}+\mathrm{H}$ as a function of the $\bar{d}$ kinetic energy per nucleon.

We stick to the empirical approach by using the cross section given in Ref. [8]. The total inelastic nonannihilating cross section $\sigma^{\bar{d}+p}_{\text{inel,non-ann}}$ (NAR in Ref. [8]) is obtained by summing up the $\bar{p} + d \longrightarrow (n\pi)\bar{p}d$ cross sections which are experimentally available. As seen in Fig. 16 (black solid line), the cross section peaks at ≈ 4 mb. As no attempt was made to evaluate the (expectedly small) contributions of the channels not known experimentally, the overall evaluation is a lower bound [8]. In the same Fig. 16, for reference purposes, we show all the cross sections used in this paper.

The last issue is the energy redistribution of the non-annihilated $\bar{d}$. In most of the papers dealing with antinuclei (e.g., [1,20,28]), the energy distribution of the surviving particles is based on the limiting fragmentation hypothesis (see references in [8]):

$$\frac{d\sigma^{\bar{d}\mathrm{H}\to\bar{d}X}}{dE_k}(E'_k \longrightarrow E_k) = \frac{\sigma^{\bar{d}\mathrm{H}}_{\text{inel,non-ann}}}{E'_k}. \tag{A3}$$

However, experimentally, the $pp \longrightarrow pX$ differential cross section was shown to be largely independent of the longitudinal momentum p^*_l of the produced particles in the center of mass and can be written in the laboratory frame as [92]:

$$\frac{d^2\sigma(pp \longrightarrow pX)}{dpd\Omega} = \frac{p^2}{2\pi p_t}\frac{\gamma(E - \beta p\cos\theta)}{E} \times 610 p_t^2 \exp\left[-\frac{p_t}{0.166}\right] \tag{A4}$$

where γ and β are the usual Lorentz factor and particle velocity, and p_t the transverse momentum of the particle. Following Duperray *et al.* [8], the same functional form is used for $\bar{d}$ and we define

$$\frac{d\sigma^{\text{Anderson}}}{dE_k} \equiv \int_\theta^{2\pi} \frac{d^2\sigma(pp \longrightarrow pX)}{dpd\Omega}\sin\theta d\theta. \tag{A5}$$

Note that an incorrect normalization was applied in Ref. [8] for the final cross section. The differential cross section for the tertiary term reads

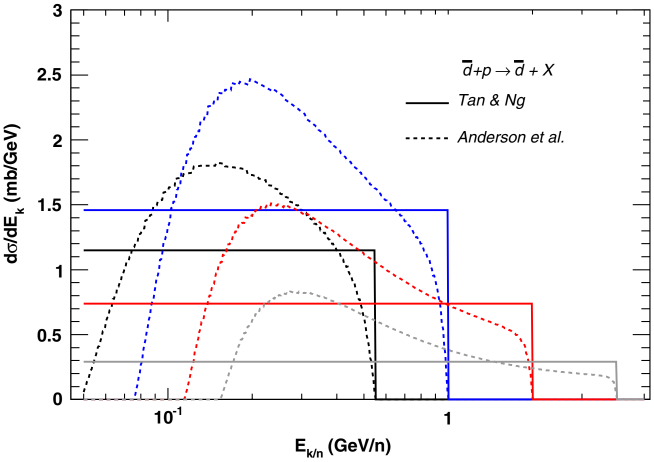

FIG. 17 (color online). Differential redistribution cross section $\bar{d} + p \longrightarrow \bar{d} + X$ as a function of the $\bar{d}$ kinetic energy per nucleon. Solid curves are for the limiting fragmentation hypothesis as used, e.g., in Tan and Ng [94] and dashed curves are for the Anderson *et al.* parameterization [92]. The four sets of curves correspond to four incident $\bar{d}$ energy: 0.55 GeV/n (black), 1 GeV/n (blue), 2 GeV/n (red) and 4 GeV/n (gray).

$$\frac{d\sigma^{\bar{d}\mathrm{H}\to\bar{d}X}}{dE_k}(E'_k \longrightarrow E_k) = \sigma^{\bar{d}\mathrm{H}}_{\text{inel,non-ann}}\left[\frac{d\sigma^{\text{Anderson}}}{dE_k}\right] \cdot \left[\int_0^{E'_k}\frac{d\sigma^{\text{Anderson}}}{dE''_k}dE''_k\right]^{-1}. \tag{A6}$$

Note, however, that this correction does not change significantly the tertiary spectrum and conclusions given in Ref. [8]. The inelastic scattering spectra in the laboratory for 0.55 (black), 1 (blue), 2 (red) and 4 GeV/n (gray) $\bar{d}$ are shown in Fig. 17. For each of these energies, the Anderson *et al.* [92] scheme more efficiently redistributes $\bar{d}$ at very low energy (a few hundreds of MeV), as compared with the other one.

Finally, we have not yet discussed the $\bar{d}$ + He cross sections. Here, for the total, elastic, nonannihilating cross section, we simply use the naive geometrical factor $A^{2/3}$ to account for interaction on He gas in the ISM:

$$\sigma^{\bar{d}+\mathrm{He}} \approx 2.52\sigma^{\bar{d}+\mathrm{H}}. \tag{A7}$$

The same factor is also assumed for the differential tertiary cross section.

[1] F. Donato, N. Fornengo, and P. Salati, Phys. Rev. D **62**, 043003 (2000).
[2] K. Mori, C. J. Hailey, E. A. Baltz, W. W. Craig, M. Kamionkowski, W. T. Serber, and P. Ullio, Astrophys. J. **566**, 604 (2002).
[3] C. J. Hailey, W. W. Craig, F. A. Harrison, J. Hong, K. Mori, J. Koglin, H. T. Yu, and K. P. Ziock, Nucl. Instrum. Methods Phys. Res., Sect. B **214**, 122 (2004).
[4] C. J. Hailey, T. Aramaki, W. W. Craig, L. Fabris, F. Gahbauer, J. E. Koglin, N. Madden, K. Mori, H. T. Yu, and K. P. Ziock, J. Cosmol. Astropart. Phys. 01 (2006) 7.
[5] L. Arruda, F. Barão, and R. Pereira, arXiv:0710.0993.

[6] H. Fuke, T. Maeno, K. Abe, S. Haino, Y. Makida, S. Matsuda, H. Matsumoto, J.W. Mitchell, A.A. Moiseev, J. Nishimura *et al.*, Phys. Rev. Lett. **95**, 081101 (2005).

[7] P. Chardonnet, J. Orloff, and P. Salati, Phys. Lett. B **409**, 313 (1997).

[8] R. Duperray, B. Baret, D. Maurin, G. Boudoul, A. Barrau, L. Derome, K. Protasov, and M. Búenerd, Phys. Rev. D **71**, 083013 (2005).

[9] 'V.S. Berezinskii, S.V. Bulanov, V.A. Dogiel, and V.S. Ptuskin, *Astrophysics of Cosmic Rays*, edited by V.L. Ginzburg (North-Holland, Amsterdam, 1990).

[10] K. Mannheim and R. Schlickeiser, Astron. Astrophys. **286**, 983 (1994).

[11] I. V. Moskalenko and A. W. Strong, Astrophys. J. **493**, 694 (1998).

[12] E. S. Seo and V. S. Ptuskin, Astrophys. J. **431**, 705 (1994).

[13] U. Heinbach and M. Simon, Astrophys. J. **441**, 209 (1995).

[14] D. Maurin, F. Donato, R. Taillet, and P. Salati, Astrophys. J. **555**, 585 (2001).

[15] A. W. Strong and I. V. Moskalenko, Astrophys. J. **509**, 212 (1998).

[16] V. L. Ginzburg and S. I. Syrovatskii, *The Origin of Cosmic Rays* (Pergamon Press, New York, 1964).

[17] V.L. Ginzburg, I.M. Khazan, and V.S. Ptuskin, Astrophys. Space Sci. **68**, 295 (1980).

[18] W.R. Webber, M.A. Lee, and M. Gupta, Astrophys. J. **390**, 96 (1992).

[19] F. Donato, D. Maurin, and R. Taillet, Astron. Astrophys. **381**, 539 (2002).

[20] F. Donato, D. Maurin, P. Salati, A. Barrau, G. Boudoul, and R. Taillet, Astrophys. J. **563**, 172 (2001).

[21] F. Donato, N. Fornengo, D. Maurin, P. Salati, and R. Taillet, Phys. Rev. D **69**, 063501 (2004).

[22] A. Barrau, P. Salati, G. Servant, F. Donato, J. Grain, D. Maurin, and R. Taillet, Phys. Rev. D **72**, 063507 (2005).

[23] Y. Sendouda, K. Kohri, S. Nagataki, and K. Sato, Phys. Rev. D **71**, 063512 (2005).

[24] D. Maurin, R. Taillet, and F. Donato, Astron. Astrophys. **394**, 1039 (2002).

[25] D. Maurin, R. Taillet, F. Donato, P. Salati, A. Barrau, and G. Boudoul, arXiv:astro-ph/0212111.

[26] A. Barrau, G. Boudoul, F. Donato, D. Maurin, P. Salati, and R. Taillet, Astron. Astrophys. **388**, 676 (2002).

[27] A. Barrau, G. Boudoul, F. Donato, D. Maurin, P. Salati, I. Stéfanon, and R. Taillet, Astron. Astrophys. **398**, 403 (2003).

[28] L. Bergström, J. Edsjö, and P. Ullio, Astrophys. J. **526**, 215 (1999).

[29] S. T. Butler and C. A. Pearson, Phys. Rev. **129**, 836 (1963).

[30] A. Schwarzschild and Č. Zupančič, Phys. Rev. **129**, 854 (1963).

[31] G. Gustafson and J. Hakkinen, Z. Phys. C **61**, 683 (1994).

[32] M.C. Lemaire, S. Nagamiya, S. Schnetzer, H. Steiner, and I. Tanihata, Phys. Lett. **85B**, 38 (1979).

[33] S. Datta, R. Caplar, N. Cindro, R.L. Auble, J.B. Bazll, and R.L. Robinson, J. Phys. G **14**, 937 (1988).

[34] R. Duperray, Ph.D. thesis, Université Joseph Fourier, 2004, http://tel.archives-ouvertes.fr/docs/00/04/70/19/PDF/tel-00006637.pdf.

[35] A. Aktas *et al.* (H1 Collaboration), Eur. Phys. J. C **36**, 413 (2004).

[36] S. Chekanov *et al.* (ZEUS Collaboration), Nucl. Phys. **B786**, 181 (2007).

[37] S. Schael *et al.* (ALEPH Collaboration), Phys. Lett. B **639**, 192 (2006).

[38] D.M. Asner *et al.* (CLEO Collaboration), Phys. Rev. D **75**, 012009 (2007).

[39] R. Arsenescu, C. Baglin, H.P. Beck, K. Borer, A. Bussière, K. Elsener, P. Gorodetzky, J.P. Guillaud, S. Kabana, R. Klingenberg *et al.*, New J. Phys. **5**, 150 (2003).

[40] M.G. Albrow *et al.* (CHLM Collaboration), Nucl. Phys. **B97**, 189 (1975).

[41] W.M. Gibson *et al.* (British-Scandinavian-MIT Collaboration), Lett. Nuovo Cimento Soc. Ital. Fis. **21**, 189 (1978).

[42] V. V. Abramov *et al.*, Sov. J. Nucl. Phys. **45**, 845 (1987).

[43] T. Sanuki, M. Motoki, H. Matsumoto, E.S. Seo, J.Z. Wang, K. Abe, K. Anraku, Y. Asaoka, M. Fujikawa, M. Imori *et al.*, Astrophys. J. **545**, 1135 (2000).

[44] J. Alcaraz, D. Alvisi, B. Alpat, G. Ambrosi, H. Anderhub, L. Ao, A. Arefiev, P. Azzarello, E. Babucci, L. Baldini *et al.*, Phys. Lett. B **472**, 215 (2000).

[45] J. Alcaraz, B. Alpat, G. Ambrosi, H. Anderhub, L. Ao, A. Arefiev, P. Azzarello, E. Babucci, L. Baldini, M. Basile *et al.*, Phys. Lett. B **490**, 27 (2000).

[46] J. Alcaraz, B. Alpat, G. Ambrosi, H. Anderhub, L. Ao, A. Arefiev, P. Azzarello, E. Babucci, L. Baldini *et al.* (), Phys. Lett. B **494**, 193 (2000).

[47] P. Picozza, A.M. Galper, G. Castellini, O. Adriani, F. Altamura, M. Ambriola, G.C. Barbarino, A. Basili, G.A. Bazilevskaja, R. Bencardino *et al.*, Astropart. Phys. **27**, 296 (2007).

[48] M. Ave *et al.*, Astrophys. J. **678**, 262 (2008).

[49] G. Hinshaw *et al.*, arXiv:0803.0732.

[50] E. Komatsu *et al.*, arXiv:0803.0547.

[51] J. Dunkley *et al.* (WMAP Collaboration), arXiv:0803.0586.

[52] A. Bottino, F. Donato, N. Fornengo, and S. Scopel, Phys. Rev. D **77**, 127301 (2008).

[53] A. Bottino, V. de Alfaro, N. Fornengo, G. Mignola, and S. Scopel, Astropart. Phys. **1**, 61 (1992).

[54] C. Arina and N. Fornengo, J. High Energy Phys. 11 (2007) 029.

[55] H. Baer and S. Profumo, J. Cosmol. Astropart. Phys. 12 (2005) 008.

[56] A. Bottino, F. Donato, N. Fornengo, and S. Scopel, Phys. Rev. D **77**, 015002 (2008).

[57] N. Fornengo, *Proceedings of the 5th International Heidelberg Conference On Dark Matter In Astro And Particle Physics (DARK 2004)* (Springer, New York, 2007).

[58] T. Sjostrand *et al.*, Comput. Phys. Commun. **135**, 238 (2001).

[59] J. Lavalle, Q. Yuan, D. Maurin, and X.-J. Bi, Astron. Astrophys. **479**, 427 (2008).

[60] F. Donato, G. Gentile, and P. Salucci, Mon. Not. R. Astron. Soc. **353**, L17 (2004).

[61] K. Heitmann, Z. Lukic, P. Fasel, S. Habib, M.S. Warren, M. White, J. Ahrens, L. Ankeny, R. Armstrong, B. O'Shea *et al.*, arXiv:0706.1270.

[62] J.F. Navarro, E. Hayashi, C. Power, A.R. Jenkins, C.S. Frenk, S.D.M. White, V. Springel, J. Stadel, and T.R.

Quinn, Mon. Not. R. Astron. Soc. **349**, 1039 (2004).

[63] F. Stoehr, Mon. Not. R. Astron. Soc. **365**, 147 (2006).

[64] D. Merritt, A. W. Graham, B. Moore, J. Diemand, and B. Terzić, Astron. J. **132**, 2685 (2006).

[65] A. W. Graham, D. Merritt, B. Moore, J. Diemand, and B. Terzić, Astron. J. **132**, 2701 (2006).

[66] M. Ricotti, A. Pontzen, and M. Viel, Astrophys. J. **663**, L53 (2007).

[67] A. V. Macciò, B. Moore, J. Stadel, and J. Diemand, Mon. Not. R. Astron. Soc. **366**, 1529 (2006).

[68] S. Mashchenko, H. M. P. Couchman, and J. Wadsley, Nature (London) **442**, 539 (2006).

[69] J. F. Navarro, C. S. Frenk, and S. D. M. White, Astrophys. J. **490**, 493 (1997).

[70] J. Diemand, B. Moore, and J. Stadel, Mon. Not. R. Astron. Soc. **353**, 624 (2004).

[71] N. Fornengo, L. Pieri, and S. Scopel, Phys. Rev. D **70**, 103529 (2004).

[72] A. Bottino, F. Donato, N. Fornengo, and S. Scopel, Phys. Rev. D **70**, 015005 (2004).

[73] D. Maurin, R. Taillet, and C. Combet, arXiv:astro-ph/0609522.

[74] D. Maurin and R. Taillet, Astron. Astrophys. **404**, 949 (2003).

[75] V. Choutko and F. Giovacchini (AMS Collaboration), in Proceeding of the 30th International Cosmic Ray Conference, 2007 (to be published).

[76] J. E. Koglin, JOP:Conference Series, TAUP 2007 Proceedings (to be published).

[77] F. Barao and R. Pereira (private communication).

[78] C. Hayley (private communication).

[79] A. Bottino, F. Donato, N. Fornengo, and S. Scopel, Phys. Rev. D **63**, 125003 (2001).

[80] A. Bottino, N. Fornengo, G. Polesello, and S. Scopel, Phys. Rev. D **77**, 115026 (2008).

[81] A. Bottino, F. Donato, N. Fornengo, and P. Salati, Phys. Rev. D **72**, 083518 (2005).

[82] A. Bottino, F. Donato, N. Fornengo, and S. Scopel, Phys. Rev. D **69**, 037302 (2004).

[83] A. Bottino, F. Donato, N. Fornengo, and S. Scopel, Phys. Rev. D **68**, 043506 (2003).

[84] A. Bottino, N. Fornengo, and S. Scopel, Phys. Rev. D **67**, 063519 (2003).

[85] S. Orito *et al.* (BESS Collaboration), Phys. Rev. Lett. **84**, 1078 (2000).

[86] T. Maeno *et al.* (BESS Collaboration), Astropart. Phys. **16**, 121 (2001).

[87] M. Aguilar *et al.* (AMS Collaboration), Phys. Rep. **366**, 331 (2002).

[88] A. Bottino, F. Donato, N. Fornengo, and S. Scopel, Phys. Rev. D **72**, 083521 (2005).

[89] V. Berezinsky *et al.*, Astropart. Phys. **5**, 1 (1996).

[90] T. Delahaye, R. Lineros, F. Donato, N. Fornengo, and P. Salati, Phys. Rev. D **77**, 063527 (2008).

[91] J. E. Koglin, T. Aramaki, W. W. Craig, L. Fabris, F. Gahbauer, C. J. Hailey, F. J. Jou, N. Madden, K. Mori, H. T. Yu *et al.*, Nucl. Phys. B, Proc. Suppl. **173**, 75 (2007).

[92] E. W. Anderson, E. J. Bleser, G. B. Collins, T. Fujii, J. Menes, F. Turkot, R. A. Carrigan, R. M. Edelstein, N. C. Hien, T. J. McMahon *et al.*, Phys. Rev. Lett. **19**, 198 (1967).

[93] W.-M. Yao *et al.*, J. Phys. G **33**, 1 (2006), http://pdg.lbl.gov.

[94] L. C. Tan and L. K. Ng, J. Phys. G **9**, 227 (1983).